EVALUATION OF THE HEMOLYTIC PROPERTIES OF CARBON NANOMATERIALS

MARCELINA PROCYK 101, MARTA KUTWIN 102*

¹ FACULTY OF BIOLOGY AND BIOTECHNOLOGY, WARSAW UNIVERSITY OF LIFE SCIENCES, 02-776 WARSAW, POLAND.

 $^{\rm 2}$ Department of Nanobiotechnology, Institute of Biology, Warsaw University of Life Sciences, 02-786 Warsaw, Poland.

* E-MAIL: MARTA_KUTWIN@SGGW.EDU.PL

Abstract

Due to their unique physical and chemical characteristics, carbon-based nanomaterials have a high potential for use in biomedical studies. However, their interaction with blood components, particularly red blood cells (RBCs), is of concern due to potential hemolytic activity. Certain studies have demonstrated no clear risks, while others have indicated that carbon-based nanomaterials may pose health threats. The current study aimed to explore the hemolytic properties of selected carbon nanostructures characterized by distinct morphologies and surface functionalities. The examined nanomaterials included graphene oxide (GO), reduced graphene oxide (rGO), multi-walled carbon nanotubes (MWNTs), and high-purity short-walled carbon nanotubes (HPS), as well as their hydroxylated derivatives (HPS-OH and MWNT-OH). The objective was to investigate how their features affect blood compatibility and their potential toxic effects. Hemolysis assays were conducted on feline red blood cells at different concentrations, along with zeta potential, UV-Vis spectrometry, NTA, BSA adsorption, and scanning electron microscopy (SEM) analyses. Additionally, microscopic assessment of erythrocyte morphology provided visual confirmation of nanomaterial-induced alterations in cell integrity and aggregation behavior. Results show that the hemolytic activity of the studied carbon nanomaterials is dependent on their concentration, surface chemistry, charge, and aggregation properties. Understanding these relationships is important for predicting the biocompatibility of nanomaterials and guiding the safe design of carbon-containing nanostructures developed for biomedical and engineering applications.

Keywords: graphene oxide, reduced graphene oxide, multiwalled carbon nanotubes, short-walled carbon nanotubes, erythrocytes, hemolysis

Introduction

Carbon-based nanomaterials are gaining increasing interest in biomedical applications due to their diverse structures, high surface area, and exceptional mechanical prop-

[Engineering of Biomaterials 173 (2025) 13]

doi:10.34821/eng.biomat.173.2025.13

Submitted: 2025-10-17, Accepted: 2025-11-03, Published: 2025-11-14



Copyright © 2025 by the authors. Some rights reserved. Except otherwise noted, this work is licensed under https://creativecommons.org/licenses/by/4.0 erties [1,2]. Among them, graphene oxide (GO), reduced graphene oxide (rGO), multi-walled carbon nanotubes (MW), and high-purity short-walled carbon nanotubes (HPS) and their hydroxylated derivatives (HPS-OH and MW-OH) are among the most extensively studied carbon nanomaterials. Their structural diversity - ranging from 2D sheets (GO, rGO) to 1D tubular forms (MW, HPS) [3], offers flexibility in biological design [4]. Key research areas involving these nanostructures include cancer therapy [5], scaffolds for tissue engineering [6], approaches to skin tissue care and management, primarily focused on wound healing [7], gene delivery [8], and biosensing [9]. Carbon-based nanoparticles are also known for their potent antimicrobial activity. Novel allotropes of carbon, discovered over the past two decades, have been applied across various scientific fields due to their microbicidal activity [10,11].

However, consideration must be given not only to the promising applications of nanomaterials, but also to their potential risks and toxicological implications, particularly in terms of their interactions with biological systems. Hemotoxicity remains a significant concern when evaluating nanomaterials for biomedical use, as their interaction with blood components, particularly upon intravenous administration, can lead to adverse effects such as hemolysis, aggregation, or immune activation [12]. Carbon nanomaterials, whether introduced into the bloodstream unintentionally or through biomedical applications, can interact directly with blood components, including proteins, red blood cells, platelets, and the coagulation system [13]. Furthermore, interactions between plasma proteins and carbon nanostructures, specifically bovine serum albumin (BSA) used in our study, are also important in assessing hemocompatibility. Albumins, particularly bovine serum albumin (BSA), are often used as model proteins to study protein-nanomaterial interactions due to their structural similarity to human serum albumin and their abundance in plasma [14]. When a protein corona forms, it can modify the surface charge, hydrophobicity and aggregation status of the nanostructures, often reducing direct contact with the erythrocyte membrane, which has been shown to decrease hemolytic activity. [15] According to Fedel (2020), hemolysis is a key indicator of blood compatibility for carbon nanostructures, reflecting their propensity to damage RBC membranes directly [16]. Hemolytic potential varies with particle size, surface oxidation, and aggregation behavior. Fedel further highlights in the review the need for standardized assay conditions to enable meaningful comparisons across different carbon nanomaterials. In our study, we employed a standardized hemolysis assay to ensure reliable and reproducible results. Albumins, particularly BSA, are often used as model proteins to study protein-nanomaterial interactions due to their structural similarity to human serum albumin and their abundance in plasma [14]. BSA readily adsorbs on the surface of carbon nanomaterials through hydrophobic and hydrogen-bonding interactions, leading to conformational rearrangements and formation of stable nanocomplexes [17]. Recent molecular simulation and radiotracer studies have demonstrated that the adsorption of BSA on single-walled carbon nanotubes (SWCNTs) is primarily driven by hydrophobic interactions and π – π stacking, accompanied by hydrogen bonding between charged amino acid residues and the polarized sp2 carbon surface [14]. The formation of such complexes significantly alters the ζ-potential of CNTs (from approximately -10 to -16 mV) and thus affects their colloidal stability and biological behavior [14]. From a biomedical standpoint, these interactions are highly relevant because the protein corona can either mitigate or exacerbate hemolytic effects,

depending on its composition and stability [16]. Previous studies have demonstrated that the presence of adsorbed albumin can reduce the direct interaction of nanomaterials with erythrocyte membranes, thereby lowering hemolytic activity and improving hemocompatibility [16]. Conversely, unstable or partial protein coatings may promote aggregation, mechanical membrane disruption, or oxidative stress, leading to morphological alterations in RBCs such as echinocyte or spherocyte formation.

We hypothesize that the hemolytic and cytotoxic effects of carbon nanomaterials are strongly dependent on their surface functionalization (e.g., hydroxylation) and concentration-dependent colloidal behavior. Thus, the present study aims to systematically compare a panel of carbon nanomaterials (GO, rGO, MWCNT, MW-OH, HPS, and HPS-OH) in terms of hemolytic activity, protein adsorption (using the BSA model), and morphological effects on erythrocytes. By correlating physicochemical characterization with biological outcomes, we seek to identify design principles for safer carbon nanomaterials in biomaterial and medical applications.

Materials and Methods

Ethical statement

The feline blood samples used in this study were collected as residual biological material from routine veterinary diagnostic procedures and classified as biological waste. Since the samples were obtained post-analysis and involved no additional handling or treatment of animals, the study did not require approval from the institutional animal ethics committee, in accordance with the Polish Act of 15 January 2015 on the Protection of Animals Used for Scientific or Educational Purposes (Journal of Laws 2015, item 266, as amended).

Blood samples

Whole blood samples from domestic cats (Felis catus) were used for the hemolysis and erythrocyte morphology assays. The samples were obtained as residual material from routine veterinary laboratory diagnostics and classified as biological waste. No animals were subjected to any experimental procedures or sacrificed specifically for this study. Following collection, the blood was stored in EDTA-coated tubes to prevent coagulation and used within 24 hours of collection. Prior to experimentation, samples were visually inspected to confirm the absence of clots or hemolysis. All handling was performed under sterile conditions at room temperature. The use of feline blood as a model system was justified by its distinct osmotic and membrane fragility characteristics, which make feline erythrocytes a sensitive model for assessing hemolytic effects and nanoparticle-induced membrane alterations.

Nanomaterials and sample preparation

To evaluate hemolytic properties, six types of carbon nanoparticles were used: graphene oxide (GO), reduced graphene oxide (rGO), multi-walled carbon nanotubes 95%, <8nm (MW), multi-walled carbon nanotubes -OH 95%, <8nm (MW-OH), high-purity short-walled carbon nanotubes 98+%, <8nm (HPS), high-purity short-walled carbon nanotubes -OH 98+%, <8nm (HPS-OH). GO and rGO were purchased from the Institute of Electronic Materials Technology (Warsaw, Poland); however, MW and HPS and their hydroxylated derivatives were provided by SkySpring Nanomaterials (Houston, TX, USA). Samples were prepared at concentrations of 2.5, 5, 10, 25, 50, and 100 µg/ mL in sterile conditions under a laminar hood.

Dynamic Light Scattering and Zeta Potential

Particle size measurements were conducted at 25°C using a Zetasizer ZSP, employing dynamic light scattering (DLS) and laser Doppler velocimetry. Prior to analysis, the nanoparticle suspensions were homogenized by ultrasonication using a probe sonicator for 5 minutes to ensure uniform dispersion. All measurements were conducted in triplicate to ensure reproducibility and statistical reliability.

Zeta potential (ζ) reflects the surface charge of nanotubes in aqueous dispersions and serves as a key physical parameter for evaluating how surfactants influence the dispersion behavior and stability of surfactant-CNT systems. [16] The zeta potential was measured using the Smoluchowski approximation with a Zetasizer ZSP. Each sample was measured after an equilibration period of 120 seconds at 25°C. All measurements were repeated four times to increase credibility. For the BSA-nanoparticle interaction studies, two experimental conditions were prepared. In the first setup, 0.975 mL of BSA solution (1 mg/ mL) was mixed with 0.025 mL of nanoparticle suspension (25 μg/mL), resulting in a lower nanoparticle-to-protein ratio. In the second setup, 0.9 mL of BSA solution (1 mg/ mL) was combined with 0.1 mL of nanoparticle suspension (100 µg/mL), providing a higher nanoparticle content while maintaining the same protein concentration. Mixtures were subjected to zeta potential measurements to evaluate the effect of BSA adsorption on surface charge and colloidal stability.

Nanoparticle Tracking Analysis (NTA)

NTA measurements were performed in a NanoSight NS300 (Malvern Panalytical, Malvern, UK), equipped with a sample chamber and 488 nm laser.

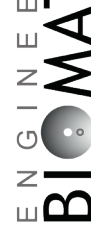
For the NTA measurements, carbon nanoparticle suspensions at concentrations of 25 µg/mL and 100 µg/mL were analyzed. The samples were introduced into the instrument chamber using sterile syringes. During analysis, numerous individual particles were tracked in real time based on their Brownian motion, and particle size was calculated by the software using the Stokes-Einstein equation.

UV-Vis Spectrophotometry

Ultraviolet-visible (UV-Vis) relies on the absorption of electromagnetic radiation in the ultraviolet (200-400 nm) and visible (400-800 nm) regions by π -electron systems, enabling the identification of characteristic optical transitions and electronic structure features specific to CNTs. [17] This technique was employed to monitor surfactantassisted stabilization, assess the CNT aggregation state, and identify characteristic absorption bands related to their electronic structure. UV-Vis spectrophotometry was employed to analyze sample absorbance across a spectral range of 230-1000 nm. Samples were prepared of appropriate solvents and transferred into clean quartz cuvettes, ensuring the absence of bubbles or particulates. The spectrophotometer was calibrated using a blank, and measurements were taken at 25 °C.

Hemolysis Assay

The effect of nanomaterials on the integrity of erythrocyte cell membranes was assessed using a hemolytic test. The hemolysis assay was performed with cat whole blood. Blood collected from healthy donors into tubes with heparin and EDTA was centrifuged (1600 rpm, 5 min), and then the plasma and leukocyte layer were removed. The erythrocyte sediment was washed three times with sterile physiological saline solution (0.9% NaCl, ratio 1:9),



and then suspended in 9 mL of NaCl solution, depending on the volume of the obtained sediment. 0.9 mL of erythrocyte suspension and 100 μ L of the appropriate nanomaterial suspension were added to Eppendorf tubes. 100 μ L of a NaCl solution was used as the negative control, while 100 μ L of a 20% Triton X-100 solution was used as the positive control. Incubation was carried out at 37°C for 60 min. After incubation, samples were centrifuged (10 min), and 200 μ L of supernatant was transferred to 96-well plates, where absorbance was measured at 405 and 540 nm. Results were expressed as a percentage of hemolysis relative to the positive control (100%). Procedure was carried out according to Kutwin et al. (2014). [18]

BSA test

Adsorption of bovine serum albumin (BSA, Thermo Scientific Pierce) on the nanomaterials was evaluated following a modified BCA-based protocol. Briefly, nanomaterial suspensions were prepared at two concentrations: $25~\mu g/mL$ and $100~\mu g/mL$ in phosphate-buffered saline (PBS, pH 7.4). To each suspension, BSA was added to achieve an initial protein concentration (C0) of 1 mg/mL in a total volume (V) of 1 mL. The mixtures were incubated for 1 hour at room temperature under gentle agitation.

Following incubation, samples were allowed to settle, and aliquots were collected separately from the upper and lower layers of the suspension. The BSA concentration remaining in solution after equilibrium (*Ceq*) was determined spectrophotometrically by measuring the absorbance at 562 nm and converting it to concentration using the calibration equation:

$$Ceq(\mu g/mL) = \frac{A - 0.3308}{0.0021}$$

The obtained *Ceq* values were converted to mg/mL by dividing by 1000.

Calculation of adsorption capacity

The amount of protein adsorbed per unit mass of nanomaterial (Γ , mg BSA/mg_{nano}) was calculated using the mass balance equation:

$$\Gamma = \frac{\left(C_0 - C_{eq}\right) \cdot V}{m_{\mathsf{nano}}}$$

where C0 is the initial BSA concentration (mg/mL), V is the solution volume (mL), and mnano is the mass of nanomaterial in the sample (mg).

Henry's isotherm analysis

For each nanomaterial and layer (upper/lower), the Γ values obtained at both nanomaterial concentrations (25 and 100 $\mu g/mL)$ were plotted as a function of Ceq. The data were fitted to Henry's adsorption model:

$$\Gamma = KH \cdot Ceq$$

where KH is Henry's constant (mL/mg). Linear regression was forced through the origin, and the determination coefficient (R^2) was calculated to assess the quality of fit.

Microscopic Evaluation of Erythrocyte Morphology Blood Smear Preparation and Staining

Blood smears were prepared on microscope slides using $5 \mu l$ of blood, then air-dried and stained using the classical Giemsa and May-Grünwald methods. The slides were

analyzed using light microscopy to assess morphological changes in the erythrocytes

Scanning Electron Microscopy (SEM)

Red blood cell (RBC) morphology was examined using scanning electron microscopy (SEM) with an FEI Quanta 200 electron microscope. Blood samples were initially rinsed with phosphate-buffered saline (PBS) and fixed in 2.5% glutaraldehyde for 1 hour. Following fixation, the samples were washed twice in 0.1 M PBS and mounted onto aluminum SEM stubs. The stubs were then incubated in a humid environment for 1 hour, rinsed again in PBS, and post-fixed with 1% osmium tetroxide for 1 hour. After rinsing with distilled water, the samples were dehydrated through a graded ethanol series. Critical point drying was carried out using liquid CO₂ in a vacuum apparatus, followed by sputter-coating with gold-palladium. SEM imaging was then performed as described by Kutwin et al. (2014).

Data Analysis and Statistics

All experimental data were analyzed using GraphPad Prism 9.0® (GraphPad Software, San Diego, CA, USA). Results are presented as mean ± standard deviation (SD) from at least three independent measurements.

For comparisons between groups, statistical significance was assessed using one-way analysis of variance (ANOVA), followed by Tukey's post hoc test for multiple group comparisons. A significance level of $p \le 0.05$ was considered statistically significant. Data visualization (histograms and line plots) was performed in GraphPad Prism, and particle size distributions were analyzed using Zetasizer Nano ZS software (Malvern Panalytical, UK) and NanoSight NTA 3.4 (Malvern Panalytical, UK).

Results and Discussions

Dynamic Light Scattering and Zeta Potential

Physicochemical characteristics of nanomaterials provide insight into their interactions with living cells. Parameters such as size distribution, as measured by DLS, and zeta potential are particularly important for understanding their biological behavior.

The measured zeta potential values (FIG. 1) reveal notable differences in surface charge and colloidal stability among the tested samples. Graphene oxide (GO) exhibited the most negative zeta potential at -50.45 mV, indicating excellent colloidal stability due to strong electrostatic repulsion between particles. In contrast, all other samples: HPS (-4.155 mV), HPS-OH (-8.315 mV), MW (-5.895 mV), MW-OH (-9.7975 mV), and rGO (-8.9125 mV) show significantly lower mean negative zeta potential values. These lower values indicate weaker repulsive forces and, consequently, moderate to poor colloidal stability, rendering these systems more susceptible to aggregation.

Reduced graphene oxide (rGO) shows a zeta potential of -8.9125 mV, significantly less negative than that of GO. This reduction is attributed to the removal of oxygencontaining functional groups during the reduction process, which decreases the surface charge density and electrostatic repulsion.

The initial measurements, conducted without BSA (Fig. 1), revealed significant differences in surface charge. GO had an exceptionally high negative zeta potential (-50.45 mV), suggesting excellent colloidal stability, while HPS, MW, MW-OH, and rGO exhibited much lower values (-4 to -10 mV), indicating poor stability and strong aggregation tendencies. Hydroxylation provided modest improvements in surface charge but did not achieve the threshold for stable dispersions (±30 mV). When nanoparticles were

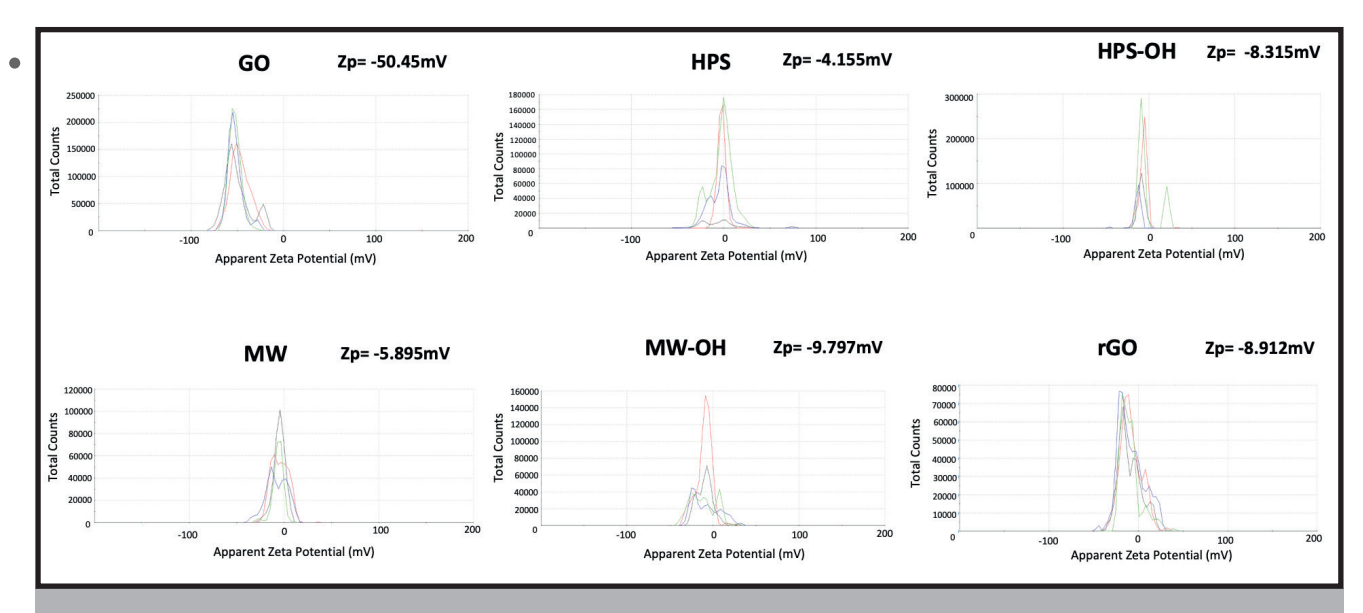


FIG. 1. Zeta potential of GO, HPS, HPS-OH, MW, MW-OH, rGO. Where Zp is the mean value of each sample's zeta potential. All measurements were performed four times.

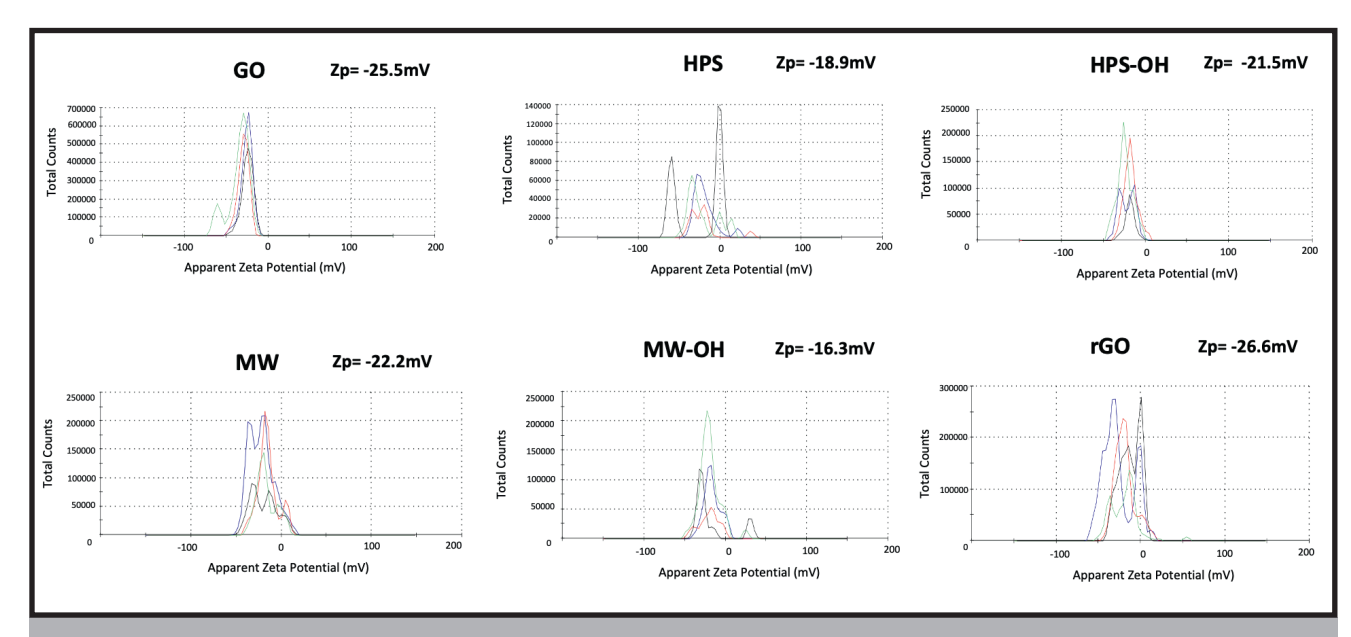


FIG. 2. Zeta potential of GO, HPS, HPS-OH, MW, MW-OH, and rGO at a concentration of 25 μ g/mL in the presence of BSA (1 mg/mL). Where Zp is the mean value of each sample's zeta potential. All measurements were performed four times.

mixed with BSA at a lower nanoparticle concentration (25 μ g/mL) (FIG. 2), the zeta potentials converged into a narrower range between -16.3 mV and -26.6 mV. This indicates that BSA adsorption alters the surface charge, partially shielding highly charged particles like GO (from -50.45 mV to -25.5 mV) but stabilizing poorly charged materials like rGO (from -8.9 mV to -26.6 mV). As a result, BSA promoted a more uniform level of moderate colloidal stability across all samples.

At the higher nanoparticle concentration (100 μ g/mL) with the same amount of BSA, the zeta potential values (FIG. 3) were again within a moderate range (-16.3 to -28.5 mV). GO maintained the most negative charge (-28.5 mV), followed closely by MW-OH (-24.7 mV), while HPS remained the least negative (-16.3 mV). Compared with the 25 μ g/mL experiment, the higher nanoparticle concentration appears to slightly enhance negative charge in most samples, possibly due to increased surface interaction between nanoparticles

and BSA molecules. Across both BSA experiments, rGO consistently benefited from protein adsorption, showing a marked improvement in stability compared to its original poor charge profile. Taken together, these results suggest that BSA acts as a stabilizing agent by adsorbing onto nanoparticle surfaces and normalizing their zeta potentials into a moderately stable range. While GO loses some of its extreme stability upon BSA addition, other materials gain enhanced stability, making BSA an effective dispersant for otherwise unstable nanoparticle systems. Surface functionalization emerged as a decisive factor influencing hemocompatibility. Hydroxylated materials, such as HPS-OH and MW-OH, exhibited reduced hemolysis compared to their non-functionalized counterparts (HPS and MWCNT). This effect is likely related to improved aqueous dispersibility and diminished hydrophobic interactions with erythrocyte membranes. Such results are in agreement with literature reports indicating that hydroxylated or polymer-coated

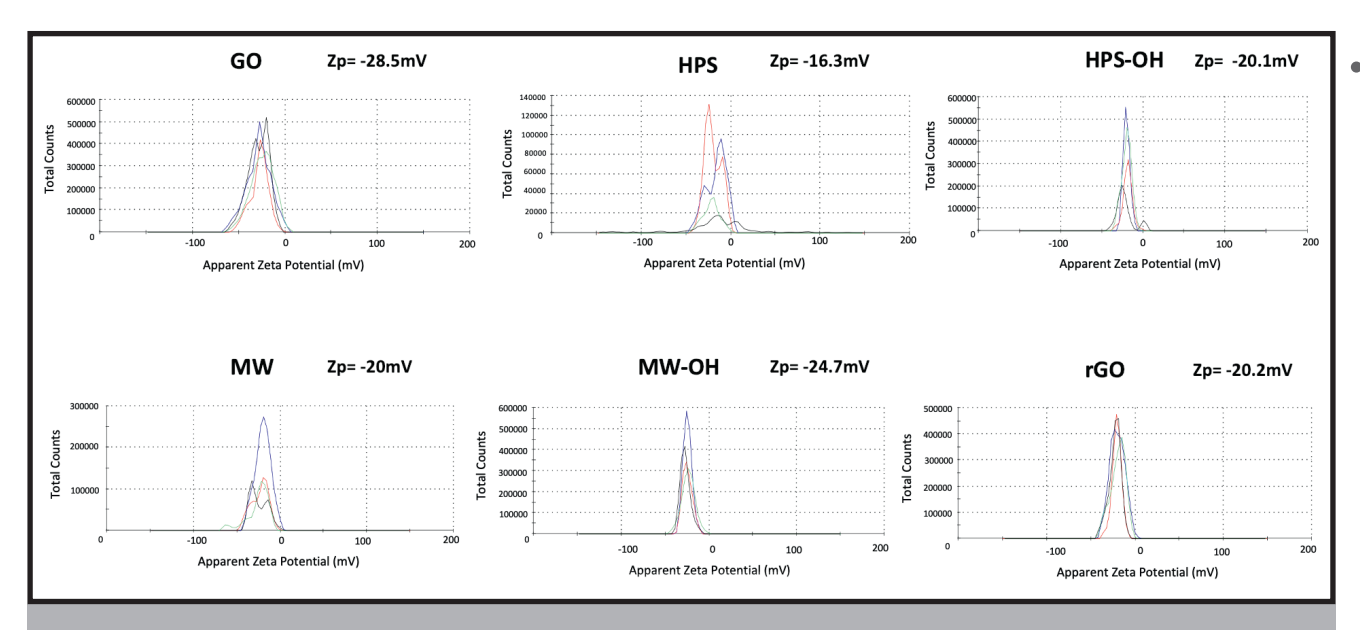


FIG. 3. Zeta potential of GO, HPS, HPS-OH, MW, MW-OH, and rGO at a concentration of 100 μ g/mL in the addition of BSA (1 mg/mL). Where Zp is the mean value of each sample's zeta potential. All measurements were performed four times.

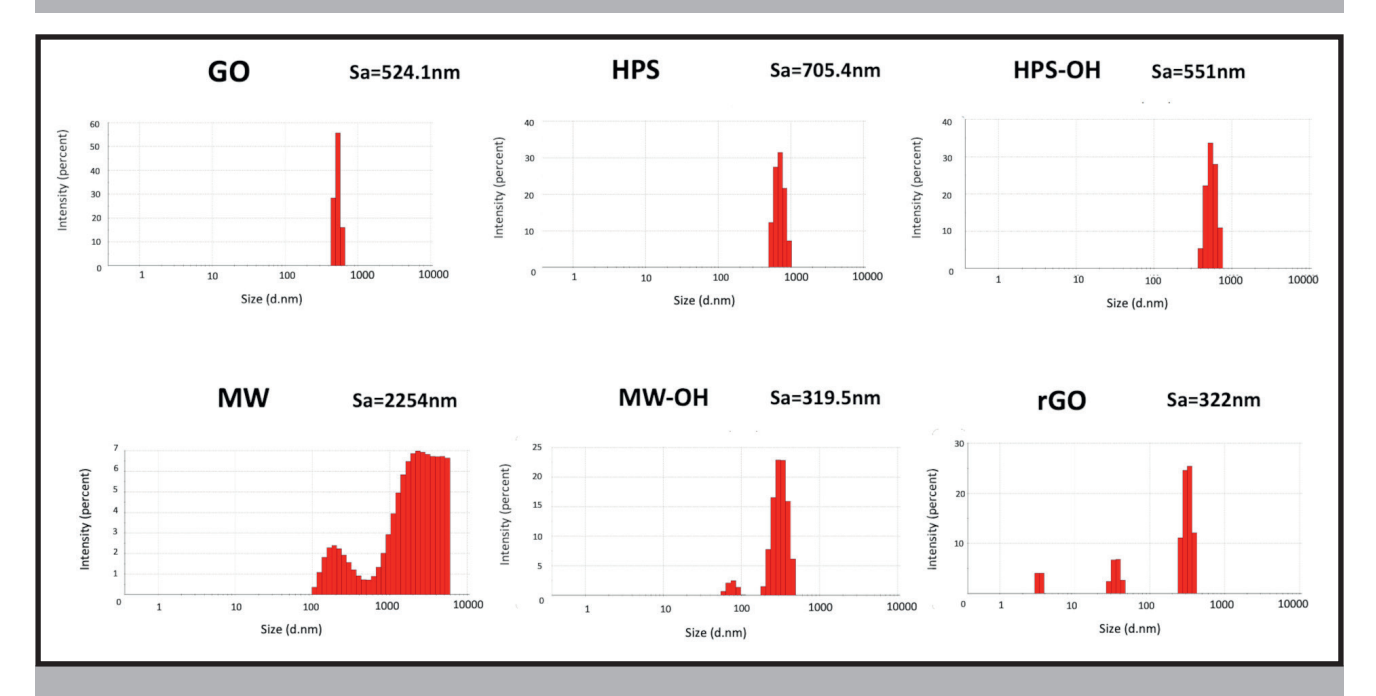


FIG. 4. Size distribution of nanomaterials used. All measurements were performed three times.

carbon nanotubes display lower hemolytic activity due to surface passivation, which shields sharp nanotube edges and facilitates the formation of a biocompatible protein corona [19]. For further analysis, concentrations of 25 μg/mL and 100 µg/mL were selected, as they produced hemolysis values within physiologically acceptable ranges. Nevertheless, a concentration-dependent increase in hemolysis was observed for most tested materials. GO showed a strongly negative zeta potential (-50.45 mV), confirming its excellent colloidal stability through strong electrostatic repulsion. Conversely, rGO, MWCNTs, and HPS-derived nanomaterials exhibited lower absolute zeta potential values (-4 to -9 mV), indicating reduced charge stabilization and a greater tendency towards aggregation. This finding is consistent with the general principle that suspensions with zeta potentials more negative than -30 mV or more positive than +30 mV are typically stable, whereas those within -30 mV to +30 mV are prone to aggregation [34].

DLS measurements (FIG. 4) revealed clear differences in particle size and distribution among the tested nanomaterials, reflecting the effect of surface modification on their colloidal behavior. Graphene oxide (GO) shows an average particle size of 524.1 nm with a narrow and uniform distribution, consistent with its highly negative zeta potential (-50.45 mV), which ensures excellent dispersion stability. Reduced graphene oxide (rGO) also showed favorable dispersion characteristics, with a relatively small average particle size of 322 nm and a narrow distribution, despite its moderate zeta potential. In contrast, hydroxylation of both MW and HPS led to improvements in dispersion. The average particle size of MW decreased from 2254 nm to 319.5 nm upon hydroxylation (MW-OH), and HPS decreased from 705.4 nm to 551 nm (HPS-OH). These reductions suggest that the introduction of hydroxyl groups enhanced surface functionalization, improving colloidal behavior by increasing electrostatic or steric

NGINEERING OF MATERIALS repulsion. DLS results support the conclusions drawn from the zeta potential data. The surface chemistry and particle size of carbon-based nanostructures—including graphene platelets, multi-walled carbon nanotubes (MWCNTs), and short-walled CNTs—are crucial determinants of their toxicity, biodistribution, and excretion

[20-21]. Consequently, different carbon-based nanomaterials can elicit markedly distinct biological responses in vivo. Consistent with previous studies, graphene oxide (GO) exhibited dose-dependent hemolysis, likely due to its high surface oxidation and strong affinity for the lipid bilayer of erythrocyte membranes [22].

Nanoparticle Tracking Analysis (NTA)

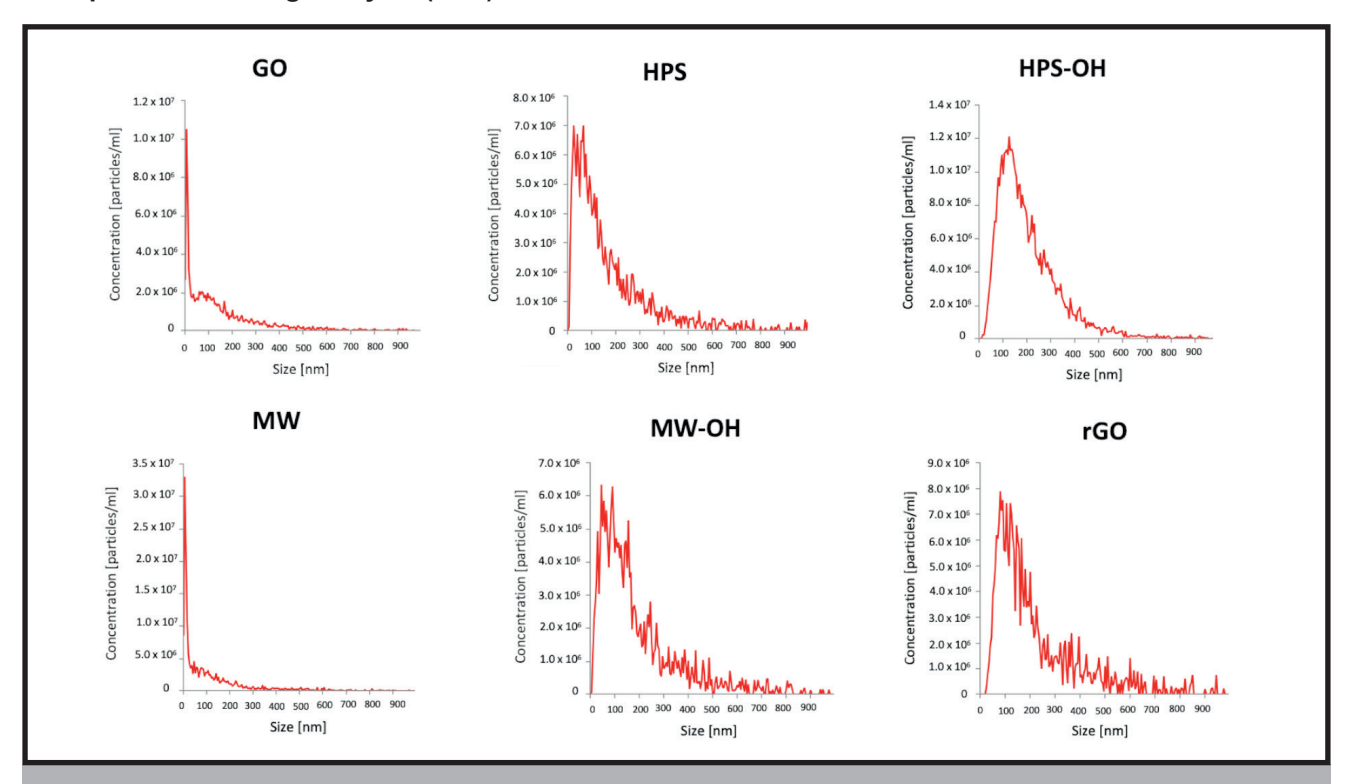


FIG. 5. Average Size Distribution of each carbon nanostructure at a concentration 25 µg/mL

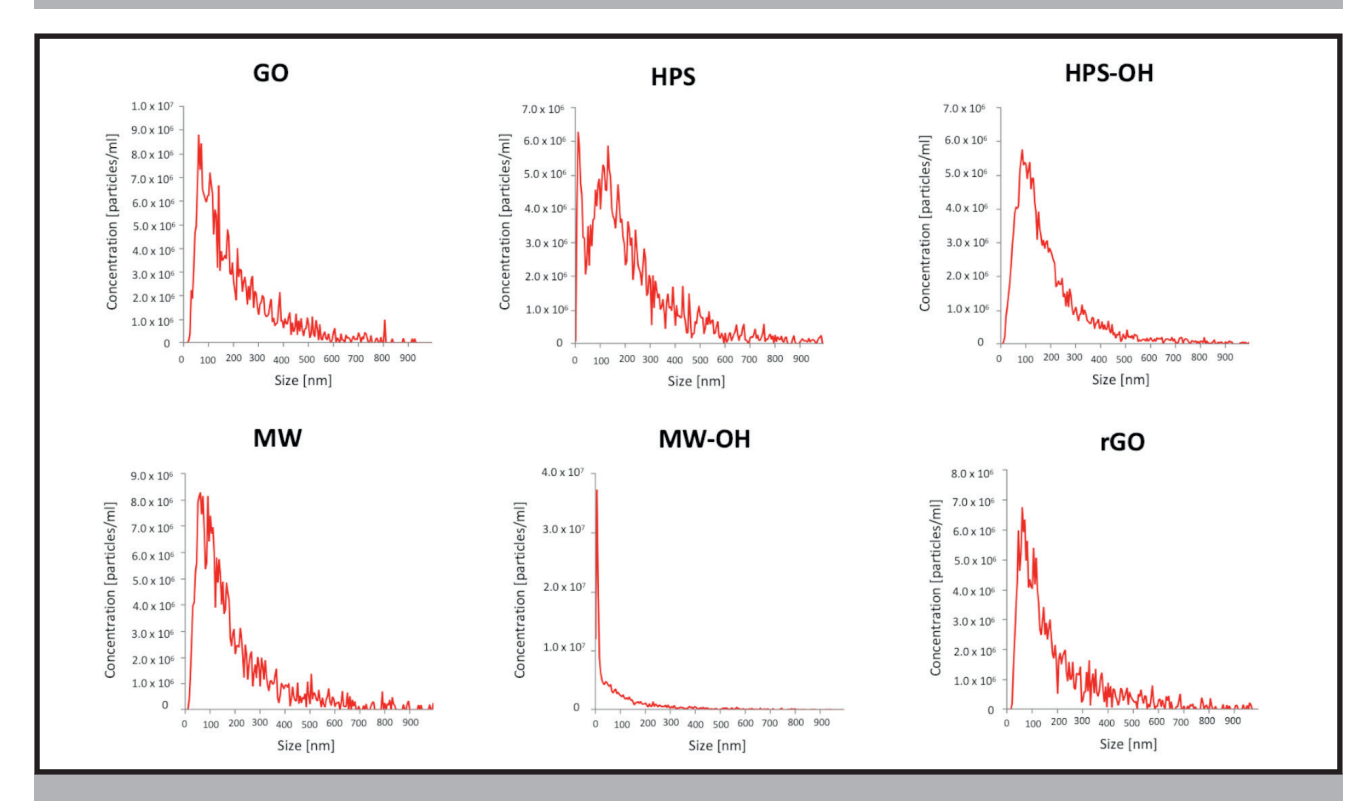


FIG. 6. Average Size Distribution of each carbon nanostructure at a concentration of 100 μg/mL

TABLE 1 NTA Beculto for	Nonoportiolo	Sucrencione	of 25 ualmi	and 100 ug/ml
TABLE 1. NTA Results for	r Nanobarticie	Suspensions	at 25 ug/ml	_ and 100 ud/mL

Type of nanoparticle	Mode [nm]	Mean [nm]	Standard deviation [nm]	Concentration [particles/ml]	D10 [nm]	D50 [nm]	D90 [nm]	Valid tracks	Span
GO 25 ug/ml	7.5	162	199	1.05 x 10 ⁸	9	101	391	5633	3.81
HPS 25 ug/ml	67.5	246	1220	2.25 x 10 ⁸	31	118	420	2669	3.29
HPS-OH 25 ug/ml	127.5	229	1303	4.80 x 10 ⁸	80	173	379	14866	1.74
MW 25 ug/ml	7.5	122	178	2.03 x 10 ⁸	7	56	329	3458	5.77
MW-OH 25 ug/ml	47.5	199	188	2.27 x 10 ⁸	45	141	432	2338	2.75
rGO 25 ug/ml	82.5	245	248	2.75 x 10 ⁸	72	165	502	1723	2.60
GO 100 ug/ml	62.5	232	242	2.77 x 10 ⁸	63	160	460	2067	2.49
HPS 100 ug/ml	12.5	470	3509	2.72 x 10 ⁸	34	173	527	5155	2.84
HPS-OH 100 ug/ml	87.5	317	3835	2.00 x 10 ⁸	63	148	403	8575	2.30
MW 100 ug/ml	62.5	203	194	2.80 x 10 ⁸	53	138	433	2028	2.75
MW-OH 100 ug/ml	7.5	112	207	2.06 x 10 ⁸	6	45	291	4029	6.31
rGO 100 ug/ml	62.5	194	173	1.92 x 10 ⁸	52	132	430	2139	2.86

DLS measurements were used to determine the hydrodynamic diameter and dispersity of the particles in aqueous suspension, while NTA enabled the quantification of particle concentration and visualization of distribution profiles at different sample dilutions (FIG. 5-6). The NTA results (TABLE 1) summarize the size distribution, concentration, and polydispersity of different carbon-based nanoparticles measured at two concentrations (25 µg/mL and 100 µg/mL) (TABLE 1). Overall, the data reveal a broad variability in mean particle sizes, ranging from 122 nm (MW 25 μ g/mL) up to 470 nm (HPS 100 μ g/mL), indicating diverse levels of heterogeneity across samples. The span values, which reflect distribution width, vary substantially: some samples, such as MW 25 µg/mL (5.77) and MW-OH 100 µg/mL (6.31), show highly polydisperse populations, while others, like HPS-OH 25 µg/mL (1.74), are more monodisperse. Concentrations are in the order of

10⁸ particles/mL for all samples, with the highest values observed for HPS-OH 25 µg/mL (4.80 × 10⁸ particles/mL). Increasing the nanoparticle concentration from 25 µg/mL to 100 µg/mL did not always result in proportional increases in mean size or concentration, suggesting differences in aggregation behavior and stability among the materials. For example, GO exhibited consistent sizes between the two concentrations (162 nm vs. 232 nm), whereas HPS showed a shift from 246 nm at 25 µg/mL to 470 nm at 100 μg/mL, indicating strong aggregation tendencies. Comparative diagrams (FIG. 7) illustrate the differences in particle size distributions across the tested nanomaterials and concentrations. Panels (A-F) highlight the influence of surface chemistry and concentration on aggregation behavior and colloidal stability, revealing distinct differences between graphene-based and polymeric systems, as well as between hydroxylated and non-hydroxylated forms.

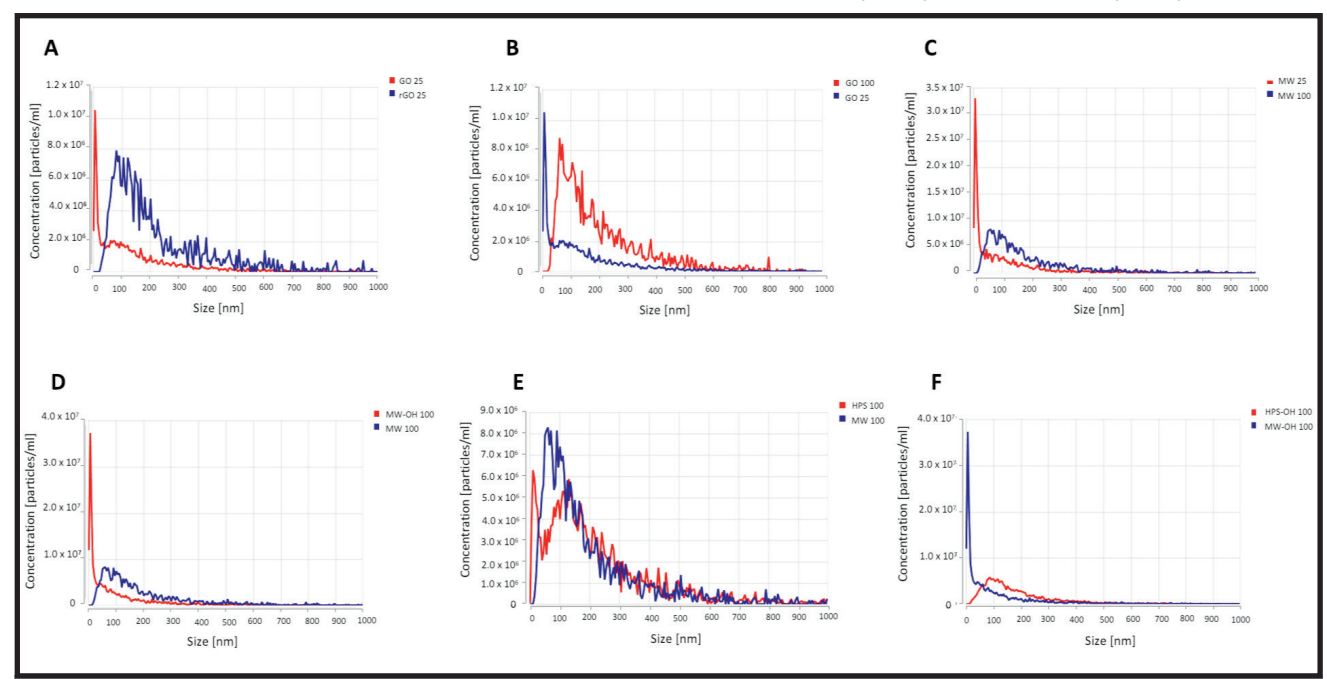


FIG. 7. Comparative diagrams of average size distribution where: (A) GO vs rGO, (B) GO 100 vs 25 μ g/mL, (C) MW 100 vs 25 μ g/mL, (D) MW-OH vs MW, (E) HPS vs MW, (F) HPS-OH vs MW-OH

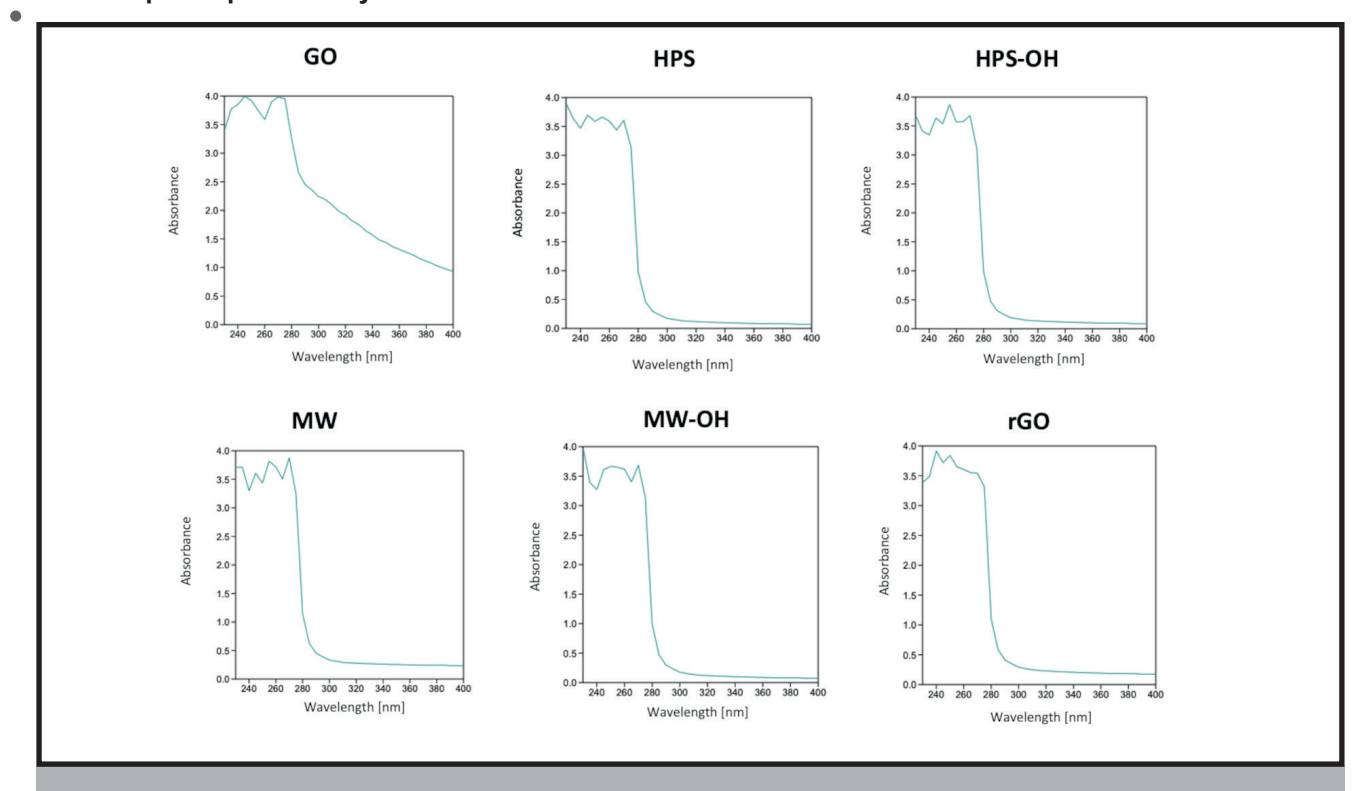


FIG. 8. Diagrams of UV-Vis spectrometry of each carbon nanoparticle

Typically, GO shows a prominent absorption peak around 231-233 nm, attributed to $\pi \to \pi^*$ transitions of aromatic C-C bonds. Additionally, a shoulder appears near 300 nm, corresponding to n \rightarrow π^* transitions of C=O bonds. [23] In rGO, this absorption peak undergoes a redshift, appearing at approximately 257 nm. This shift denotes the partial restoration of the π -conjugated system as oxygen functional groups are removed during the reduction of GO to rGO. [24] MWCNTs typically display an absorption peak around 260 nm in their UV-Vis spectra. This peak is attributed to the $\pi\text{-plasmon}$ resonance of the graphitic structure. [25] Upon hydroxyl functionalization, this peak often shifts slightly, with MWCNTs-OH displaying an absorption peak at approximately 270 nm. This shift indicates modifications in the electronic structure due to the introduction of hydroxyl groups. [26] In the case of HPS, the peak was observed

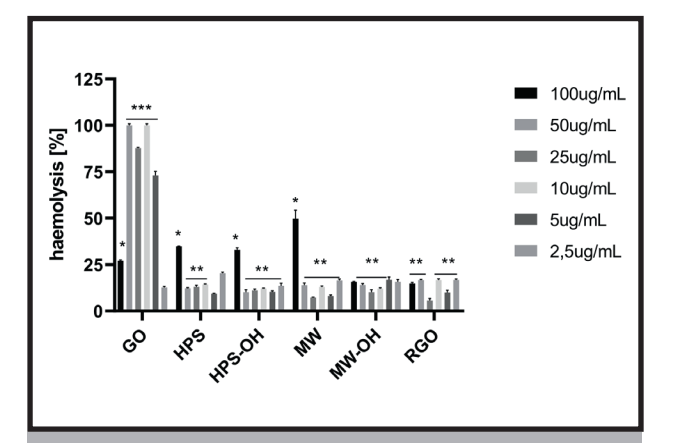


FIG. 9. Hemolytic activity of carbon-based nanomaterials at two concentrations (25 µg/mL and 100 µg/mL). Data are expressed as mean ± SD (n = 3). Asterisks (*) indicate statistically significant differences between groups (p \leq 0.05).

at around 250nm, and in HPS CNT-OH, at 275nm, which signifies its similarity to MWCNT and how hydroxyl functionalization affects both of these nanostructures.

Hemolytic Activity

Following the physicochemical characterization, the hemolytic activity of the nanomaterials was examined to determine their blood compatibility and assess whether surface modifications influence erythrocyte membrane integrity. The percentage of hemolysis (FIG. 9) was calculated by dividing the absorbance of the given sample by the absorbance of the positive control.

For further examination, samples at concentrations of 100 μg/mL and 25 μg/mL were chosen. These two yielded hemolysis values falling within physiologically accepted thresholds (i.e., <5% non-hemolytic, 5-25% mildly hemolytic, >25% hemolytic), which aligns with established hemocompatibility criteria described by Dobrovolskaia et al. (2008) [27]. Conditions yielding 100% hemolysis, as observed in 50µg/mL and 10µg/mL, may indicate absorbance saturation or non-specific interactions, as previously noted in hemolysis studies involving nanoparticles with high optical density or aggregation tendencies. [27] It is worth mentioning that some nanomaterials, especially those with a high specific surface area or a tendency to form aggregates (e.g., graphene, metal oxides, fullerenes), can spontaneously absorb light or opalize the solution, which can be misinterpreted as an increase or decrease in hemolysis. The rGO showed lower hemolytic activity, attributed to its reduced oxidation state and greater tendency to aggregate into larger clusters, which decreases direct contact with red blood cell (RBC) membranes but may still cause mechanical membrane disruption in certain contexts [28]. Additionally, interaction with proteins present in blood (formation of so-called corona proteins) can alter both the bioactivity of the materials and their effect on the test's optical system. These phenomena can lead to false-positive or false-negative results. [29]



BSA Test

To complement the hemocompatibility assessment, the interaction of nanomaterials with serum proteins was examined using the bovine serum albumin (BSA) adsorption assay. This test provides valuable insight into the protein corona formation process, which plays a crucial role in determining the behavior of nanoparticles in biological environments. The coefficient of determination ($R^2 = 0.9837$) indicated an excellent fit of the standard curve, confirming the reliability and accuracy of the BSA assay for quantitative analysis. Samples were mixed with nanoparticles at concentrations of 100 µg/mL and 25 µg/mL. After that, the upper and lower layers of the experimental samples were collected, ensuring a comprehensive analysis of protein-nanoparticle interactions. After incubation with BSA (1 mg/mL), the mixtures were separated into upper and lower fractions to distinguish between unbound and adsorbed protein (TABLE 2). The absorbance of each layer was recorded, and BSA concentration was calculated (TABLE 3) based on the standard calibration curve equation (Absorbance - 0.3308)/0.0021,

TABLE 2. Absorbance values of BSA (1 mg/mL) in upper and lower layers after incubation with carbon-based nanomaterials at two concentrations (25 µg/mL and 100 µg/mL). Measurements were performed in triplicate, and data are expressed as mean absorbance values.

Material	Concentration of nanoparticle [lg/mL]	Layer	Absorbance
GO	100	upper	0.4832333
HPS	100	upper	1.108633
HPS-OH	100	upper	0.576933
MW	100	upper	0.8989
MW-OH	100	upper	0.9379
RGO	100	upper	0.955267
GO	25	upper	1.0678
HPS	25	upper	0.669167
HPS-OH	25	upper	2.1771
MW	25	upper	2.3041
MW-OH	25	upper	1.980233
RGO	25	upper	1.817567
GO	100	lower	2.1868
HPS	100	lower	1.2679
HPS-OH	100	lower	1.211133
MW	100	lower	0.9415
MW-OH	100	lower	1.198467
RGO	100	lower	1.9224
GO	25	lower	1.9994667
HPS	25	lower	0.797567
HPS-OH	25	lower	1.1864
MW	25	lower	1.584567
MW-OH	25	lower	0.7547
RGO	25	lower	0.9366

allowing for the estimation of protein amounts associated with each nanomaterial.

Using the obtained absorbance values and the standard curve equation, the concentration of unbound BSA in each fraction was calculated to determine the amount of protein adsorbed onto the nanoparticle surface.

TABLE 3. Calculated concentration of BSA (µg/mL) in upper and lower layers following incubation with nanomaterials at two concentrations (25 µg/mL and 100 µg/mL), determined from the standard curve equation.

Material	Concentration of nanoparticle [ug/mL]	Layer	Calculated concentration of BSA [µg/mL]
GO	100	upper	72.587301
HPS	100	upper	370.3968
HPS-OH	100	upper	117.2064
MW	100	upper	270.5238
MW-OH	100	upper	289.0952
RGO	100	upper	297.3651
GO	25	upper	350.95236
HPS	25	upper	161.127
HPS-OH	25	upper	879.1905
MW	25	upper	939.6667
MW-OH	25	upper	785.4445
RGO	25	upper	707.9841
GO	100	lower	883.80953
HPS	100	lower	446.2381
HPS-OH	100	lower	419.2063
MW	100	lower	290.8095
MW-OH	100	lower	413.1746
RGO	100	lower	757.9048
GO	25	lower	794.60317
HPS	25	lower	222.2698
HPS-OH	25	lower	407.4286
MW	25	lower	597.0317
MW-OH	25	lower	201.8571
RGO	25	lower	288.4762

The BSA assay results indicate material-dependent protein binding. GO and rGO exhibited a strong affinity for BSA, with the majority of the protein detected in the lower layer, indicating significant adsorption and sedimentation. In contrast, HPS-OH exhibited high protein levels in the upper layer, possibly due to reduced binding resulting from hydrophilic surface modifications. MWCNT and MWCNT-OH exhibited moderate protein interaction. These quantitative data demonstrate material-dependent differences in BSA adsorption, reflecting how surface chemistry and hydroxyl functionalization influence protein-nanoparticle interactions. High adsorption of BSA observed for HPS and MW-OH may result from hydroxyl functionalization, which enhances hydrogen bonding and electrostatic interactions.

In contrast, GO—despite its high surface area—exhibited lower affinity in certain conditions, possibly due to hydration layers or repulsion effects at the tested pH. Differences between upper and lower sample layers likely stemmed from sedimentation phenomena, where denser aggregates in the lower fraction altered available surface area and binding geometry.

To provide a quantitative comparison of protein binding among the tested nanomaterials, the adsorption capacity (Γ) of BSA was calculated based on the measured protein concentrations in the upper and lower layers. This parameter reflects the total amount of protein adsorbed per unit mass of nanomaterial, enabling the direct evaluation of the influence of surface modification and concentration on protein–nanoparticle interactions.BSA adsorption capacity (Γ) determined for the studied nanomaterials ranged from 1.16 to 33.55 mg BSA/mg of material, depending on the nanomaterial type, layer (upper or lower), and the nanoparticle concentration in suspension (25 or 100 µg/mL) (TABLE 4.). The highest adsorption was recorded for HPS (upper layer) at 25 µg/mL (Γ ≈ approx. 33.55 mg/mg), followed by MW-OH (lower layer) at the same concentration

TABLE 4. Adsorption capacity (Γ) of BSA on different carbon-based nanomaterials at two nanoparticle concentrations (25 µg/mL and 100 µg/mL) and in two fractions (upper and lower layers).

Material	Layer	Nanoparticle con- centration (µg/mL)	Adsorption capacity (Γ) (mg/mg)
GO	upper	100	9.27
HPS	upper	100	6.30
HPS-OH	upper	100	8.83
MW	upper	100	7.29
MW-OH	upper	100	7.11
RGO	upper	100	7.03
GO	upper	25	25.96
HPS	upper	25	33.55
HPS-OH	upper	25	4.83
MW	upper	25	2.41
MW-OH	upper	25	8.58
RGO	upper	25	11.68
GO	lower	100	1.16
HPS	lower	100	5.54
HPS-OH	lower	100	5.81
MW	lower	100	7.09
MW-OH	lower	100	5.87
RGO	lower	100	2.42
GO	lower	25	8.22
HPS	lower	25	31.11
HPS-OH	lower	25	23.70
MW	lower	25	16.12
MW-OH	lower	25	31.93
RGO	lower	25	28.46

($\Gamma \approx$ approx. 31.93 mg/mg). In contrast, the lowest capacity was observed for GO (lower layer) at 100 μ g/mL ($\Gamma \approx$ approx. 1.16 mg/mg).

In most cases, Γ values were markedly higher at lower nanomaterial concentrations (25 µg/mL), suggesting that under dilute conditions, the number of available adsorption sites per unit mass is higher, and protein binding is less affected by nanoparticle aggregation. To further elucidate the mechanism of protein adsorption, Henry's isotherm model was applied to evaluate the relationship between the equilibrium concentration of unbound BSA (C_eq) and the adsorption capacity (Γ). This analysis allowed assessment of adsorption affinity through the determination of Henry's constants (K_H) and the corresponding coefficients of determination (R^2).

Henry's isotherm analysis (Fig.) confirmed a generally linear relationship between Γ and Ceq for the tested concentration range, with R² exceeding 0.95 for the majority of material–layer combinations TABLE 5.

TABLE 5. Henry's constants (*KH*) and determination coefficients (R^2) describing the linear relationship between equilibrium BSA concentration (Ceq) and adsorption capacity (Γ) for tested nanomaterials.

Material	Layer	KH (mL/mg)	R²
GO	upper	26.06	0.999
HPS	upper	49.91	0.969
HPS-OH	upper	4.63	0.739
MW	upper	2.57	0.836
MW-OH	upper	10.64	0.845
RGO	upper	14.27	0.924
GO	lower	7.87	0.893
HPS	lower	48.55	0.972
HPS-OH	lower	28.34	0.978
MW	lower	26.99	0.981
MW-OH	lower	37.60	0.947
RGO	lower	37.52	0.892

The highest KHK values were obtained for HPS (lower layer) and HPS (upper layer), indicating strong affinity of BSA for this surface. Conversely, GO in the lower layer exhibited the lowest KHK, which is consistent with its minimal adsorption capacity. For materials including MW-OH upper, RGO lower, R2 values below 0.90 were recorded, which may indicate more complex adsorption mechanisms involving multilayer formation or heterogeneous binding sites.

Overall, the BSA adsorption analysis demonstrated that protein—nanoparticle interactions are highly material-dependent and influenced by both concentration and surface functionalization. Hydroxylated nanomaterials, such as MW-OH and HPS-OH, generally exhibited more controlled and reversible adsorption profiles, suggesting improved colloidal stability and reduced nonspecific protein binding compared to their unmodified counterparts. To complement these findings and assess the potential impact of nanoparticle exposure on blood cell morphology, May—Grünwald—Giemsa staining and scanning electron microscopy (SEM) observations were performed. These analyses enabled direct

Morphology of RBC

To further verify the impact of nanoparticle-protein interactions on cellular responses, morphological evaluation of erythrocytes was conducted. In this study, feline whole blood was used as a model system for the hemolysis assay. The choice of cat blood (domestic cat) was motivated by its specific erythrocyte properties—particularly the membrane fragility and osmotic characteristics of feline red blood cells. These traits make them more susceptible to external stressors and thus a sensitive model for detecting hematotoxic effects, as feline erythrocytes exhibit greater osmotic fragility than human erythrocytes [30]. Such characteristics allow for early detection of hemolytic responses induced by nanomaterial exposure. While feline erythrocytes are particularly sensitive to membrane perturbations, it is important to contextualize their relevance by comparing them to human red blood cells (RBCs). Feline RBCs differ from human RBCs in several structural and biochemical aspects. Notably, they possess a higher number of sulfhydryl groups per hemoglobin molecule, making them more prone to oxidative damage under mild stress conditions [31]. Furthermore, feline spleens lack a sinusoidal architecture, reducing their ability to filter damaged erythrocytes, which allows structurally compromised RBCs to persist longer in circulation and amplify subclinical hemolytic effects. In contrast, human RBCs are more deformable and undergo efficient splenic culling, which may mitigate the visible effects of early-stage hemolysis. Despite these interspecies differences, both feline and human erythrocytes share fundamental properties regarding membrane structure and response to osmotic or oxidative insults. Thus, feline RBCs serve as a sensitive

early-detection model for hemolytic potential, especially for identifying subtle membrane alterations that may also be relevant in the human context. Our findings therefore provide valuable mechanistic insight, while future studies incorporating human RBCs are warranted to confirm translational relevance. This approach provided visual confirmation of how surface chemistry and nanoparticle concentration affect the integrity and aggregation behavior of blood cells. Microscopic examination of blood smears (FIG. 10) revealed that the surface chemistry and concentration of carbon nanostructures strongly influenced their distribution and interaction with erythrocytes. At lower concentrations, the nanomaterials were more evenly dispersed across the smear, minimizing direct contact with red blood cells and allowing better hemocompatibility. In contrast, higher concentrations led to pronounced aggregation of the nanoparticles themselves, rather than uniform dispersion. Additionally, surface functional groups such as -OH increased protein adsorption, promoting the formation of a protein corona that could block uniform distribution in the smear and reduce direct contact with red blood cells.

Microscopic examination of blood smears revealed that the surface chemistry and concentration of carbon nanostructures strongly influenced their distribution and interaction with erythrocytes.

SEM Imaging

Comparative microscopic evaluation clearly demonstrates that nanoparticle concentration and surface chemistry modulate erythrocyte-nanomaterial interactions. The presence of hydroxyl and oxygen-containing functional groups facilitated the formation of a protein corona, thereby limiting direct nanoparticle-cell contact at low doses. In contrast, higher concentrations promoted aggregation and localized particle accumulation. The erythrocyte morphologies observed through scanning electron microscopy (SEM) (FIG. 11-12) illustrate a progressive increase in membrane stress and

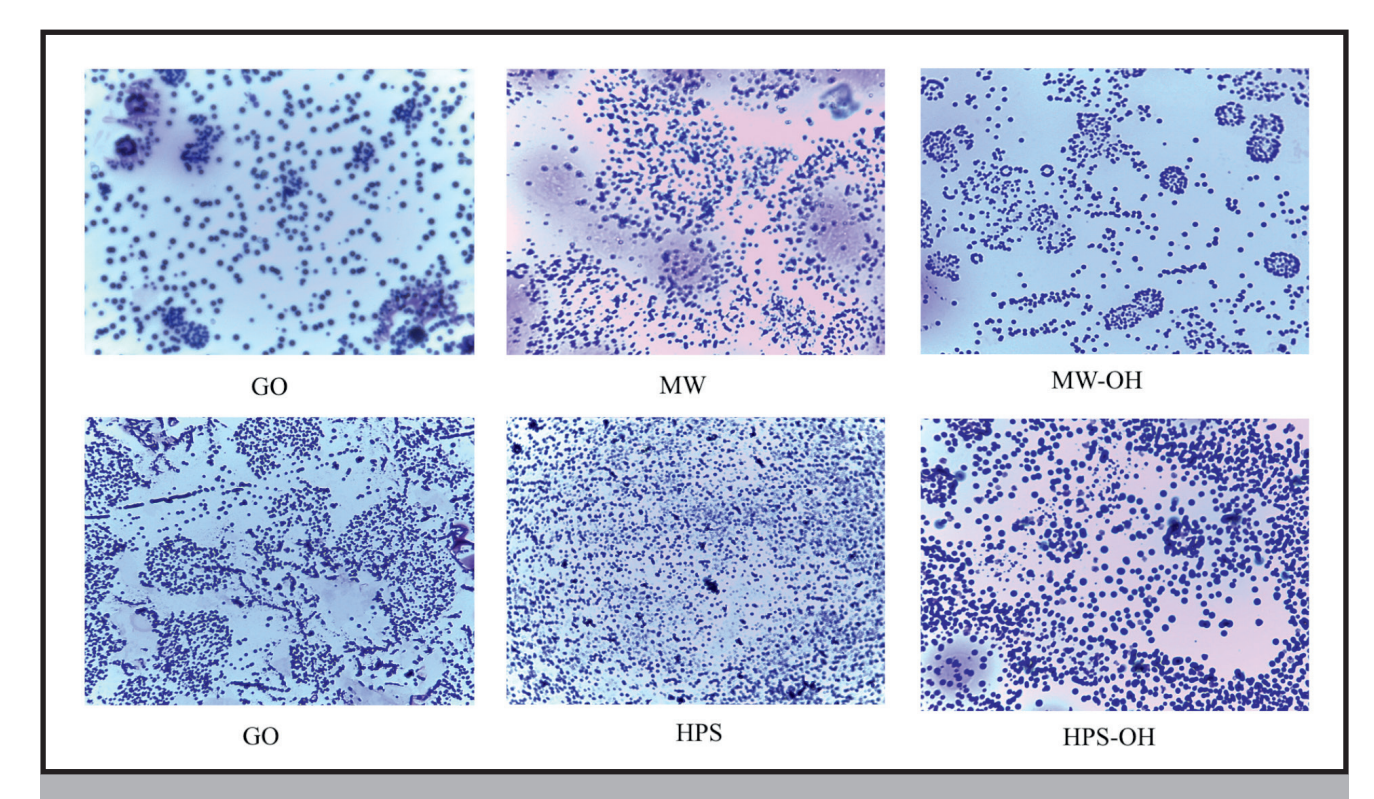


FIG. 10. Visualization of erythrocytes exposed to carbon-based nanomaterials at a concentration of 25 μg/mL upper panel and 100 μg/mL lower panel using May-Grünwald-Giemsa staining under light microscopy (1000× magnification).

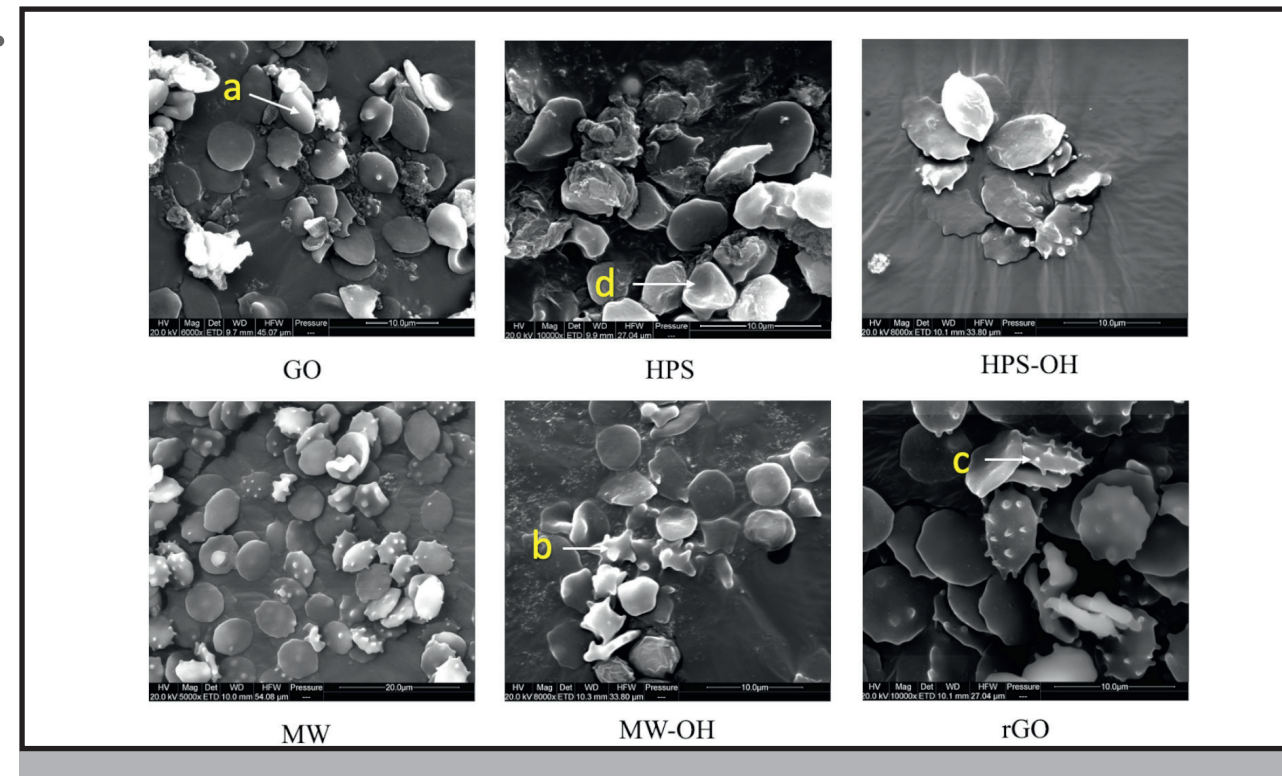


FIG. 11. Scanning electron microscopy (SEM) visualization of erythrocytes exposed to carbon-based nanomaterials at concentrations 25 µg/mL (a. echinocyte I, b. echinocyte II, c. echinocyte III, d. sphero-stomatocyte)

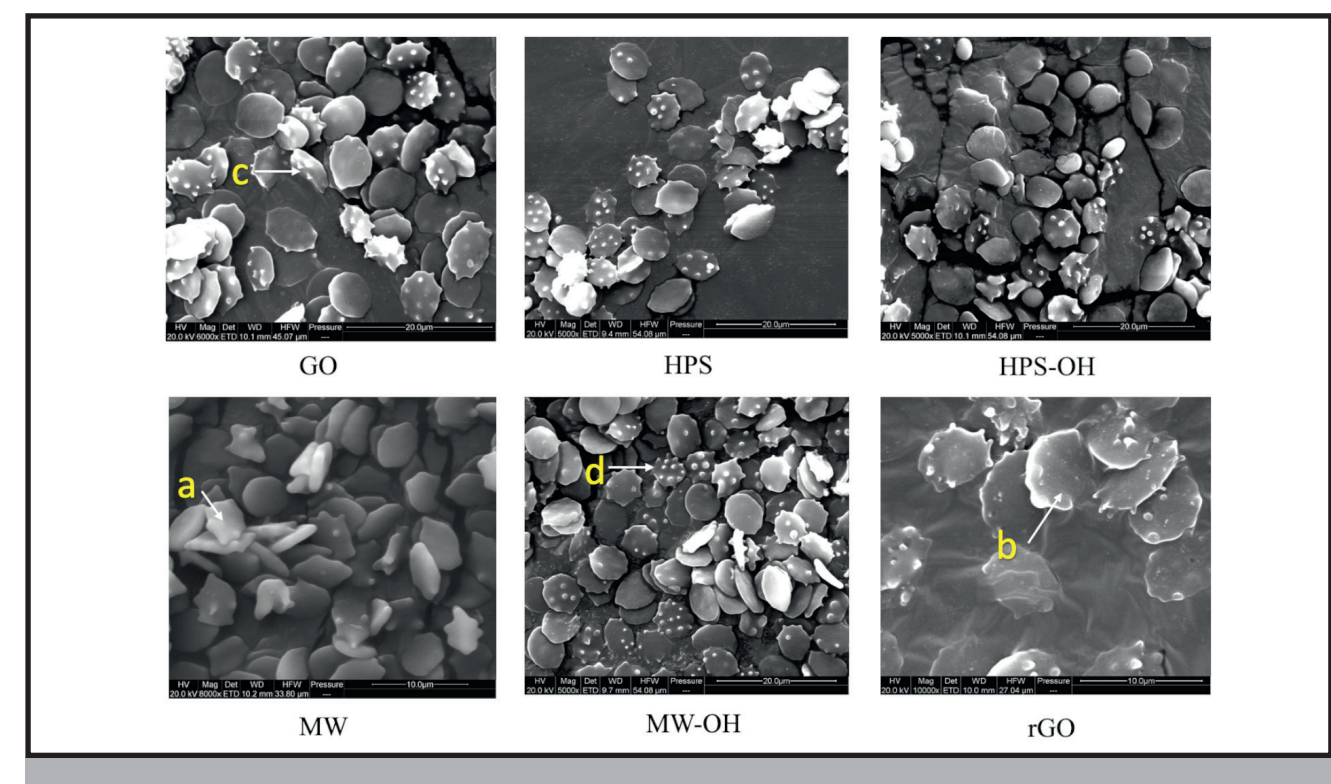


FIG. 12. Scanning electron microscopy (SEM) visualization of erythrocytes exposed to carbon-based nanomaterials at concentrations of 100 μ g/mL.

the associated risk of hemolysis. The echinocyte I shows mild membrane protrusions while largely maintaining the typical discocyte shape, which indicates minimal cellular stress. Additionally, the echinocyte II presents longer and more pronounced spicules, with visible shape distortion corresponding to moderate stress levels. The echinocyte III exhibits numerous sharp, elongated spicules and a near-

complete loss of the disc shape, signifying severe membrane deformation. Finally, the sphero-echinocyte displays a more spherical form with shorter, irregular spicules, reflecting extreme membrane damage and a high risk of hemolysis [32-35]. These morphological observations corroborate the hemolysis assay results, confirming that increasing nanoparticle concentration and surface reactivity correlate

with progressive erythrocyte membrane damage. These morphological transitions from discocytes to echinocytic and stomatocytic forms reflect the concentration-dependent effects of nanoparticle exposure. Such changes are typically associated with modifications in membrane curvature and surface tension resulting from the adsorption of nanoparticles or the formation of a protein corona. The presence of higher-order echinocyte stages (II-III) at elevated concentrations suggests enhanced surface interaction or oxidative stress, whereas the predominance of discocytes and early echinocyte I forms at lower doses indicates preserved membrane integrity and compatibility. The appearance of sphero-stomatocytes indicates a more advanced or irreversible deformation stage, likely caused by strong adhesion, oxidative stress, or mechanical effects exerted by aggregated or sharp-edged nanostructures [36]. Overall, the hemolytic behavior of carbon-based nanomaterials is dictated by multiple interrelated parameters—concentration, structure, size, shape, and surface functional groups—which collectively determine their interactions with red blood cells [37-38]. Numerous studies corroborate that physicochemical variations among carbon nanomaterials substantially modulate their hemolytic potential and blood compatibility [18, 38]. Nonetheless, some carbon nanostructures have been reported to exhibit no measurable hemolytic activity under certain conditions, underscoring the importance of experimental context and surface chemistry [39].

Conclusions

The interaction of carbon-based nanomaterials with feline erythrocytes revealed that surface chemistry and concentration are the key determinants of hemocompatibility. Incubation of GO, rGO, MWCNTs, MW-OH, HPS, and HPS-OH with red blood cells induced structural alterations of erythrocyte membranes and caused concentrationdependent hemolysis. More hydrophobic materials, such as rGO, HPS, and MWCNTs, exhibited greater hemolytic potential than their oxidized or hydroxylated counterparts (GO, MWCNT-OH, HPS-OH), which are more hydrophilic and thus display enhanced blood compatibility. All tested nanostructures triggered varying degrees of morphological deformation, including the formation of echinocyte types I-III and sphero-echinocytes, reflecting stress responses associated with nanoparticle-membrane interactions. These findings confirm that physicochemical characteristics—particularly surface functionalization, oxidation state, and colloidal stability—play a decisive role in determining biological responses to carbon nanomaterials.

In summary, surface modification and precise control of dispersion behavior are crucial strategies for minimizing hemolytic effects and enhancing the biocompatibility of carbon nanostructures. Careful physicochemical characterization and dose optimization are therefore required before considering any biomedical or therapeutic applications of these materials.

Acknowledgments

This research is an engineering diploma thesis carried out by Marcelina Procyk under the supervision of Dr. Marta Kutwin at the Department of Nanobiotechnology, Faculty of Biology and Biotechnology, Warsaw University of Life Sciences (SGGW).

This study received no financial support or external funding.

References

- [1]. Malode S.J., Pandiaraj S., Alodhayb A., Shetti N.P., Carbon nanomaterials for biomedical applications: progress and outlook. ACS Appl Bio Mater 2024;7(2):752-777. doi:10.1021/acsabm.3c00983
- [2]. Georgakilas V., Perman J.A., Tucek J., Zboril R., Broad family of carbon nanoallotropes: classification, chemistry, and applications of fullerenes, carbon dots, nanotubes, graphene, nanodiamonds, and combined superstructures. Chem Rev 2015;115:4744-4822
- [3]. Kim S.B., Kim C.H., Lee S.Y., Park S.J., Carbon materials and their metal composites for biomedical applications: a short review. Nanoscale 2024;16:16313-16328. doi:10.1039/D4NR02059F
- [4]. Gaur M., Misra C., Yadav A.B., Swaroop S., Maolmhuaidh FÓ., Bechelany M., Barhoum A., Biomedical applications of carbon nanomaterials: fullerenes, quantum dots, nanotubes, nanofibers, and graphene. Materials 2021;14:5978. doi:10.3390/ma14205978
- [5]. Mohan H., Fagan A., Giordani S., Carbon nanomaterials (CNMs) in cancer therapy: a database of CNMbased nanocarrier systems. Pharmaceutics 2023;15:1545. doi:10.3390/pharmaceutics15051545
- [6]. Kandhola G., Park S., Lim J.W., Chivers C., Song Y.H., Chung J.H., Kim J., Kim J.W., Nanomaterial-based scaffolds for tissue engineering applications: a review on graphene, carbon nanotubes and nanocellulose. Tissue Eng Regen Med 2023;20(3):411-433. doi:10.1007/s13770-023-00530-3
- [7]. Hajishoreh N.K., Jamalpoor Z., Rasouli R., Asl A.N., Sheervalilou R., Akbarzadeh A., The recent development

- of carbon-based nanoparticles as a novel approach to skin tissue care and management: a review. Exp Cell Res 2023;433(2):113821. doi:10.1016/j.yexcr.2023.113821 [8]. Yazdani S., Mozaffarian M., Pazuki G., Hadidi N., Villate-Beitia I., Zárate J., Puras G., Pedraz J.L., Carbon-based nanostructures as emerging materials for gene delivery applications. Pharmaceutics 2024;16(2):288. doi:10.3390/pharmaceutics16020288
- [9]. Askari V.R., Safaei R., Roudi H.S., Saffarian K., Moniripour A., Darbani Keshik S., Fadaei M.S., Rahimi V.B., Carbon nanostructures used in biosensors. In: Hasnain MS, Nayak AK, Aminabhavi TM (eds). Materials and Components of Biosensors in Healthcare. Academic Press; 2025. p.249-277. doi:10.1016/B978-0-443-21676-3.00015-7 [10]. Cataldo F., Da Ros T., Medicinal Chemistry and Pharmacological Potential of Fullerenes and Carbon Nanotubes. Springer, Trieste; 2008.
- [11]. Maleki Dizaj S., Mennati A., Jafari S., Khezri K., Adibkia K., Antimicrobial activity of carbon-based nanoparticles. Adv Pharm Bull 2015;5(1):19-23. doi:10.5681/ apb.2015.003
- [12]. Urbán P., Liptrott N.J., Bremer S., Overview of the blood compatibility of nanomedicines: a trend analysis of in vitro and in vivo studies. Wiley Interdiscip Rev Nanomed Nanobiotechnol 2019;11(3):e1546. doi:10.1002/
- [13]. Bussy C., Methven L., Kostarelos K., Hemotoxicity of carbon nanotubes. Adv Drug Deliv Rev 2013;65(15):2127-2134. doi:10.1016/j.addr.2013.10.008
- [14]. Bunyaev V.A., Sinolits A.V., Badun G.A., Study of carbon nanotube-bovine serum albumin interaction using the tritium radiotracer technique and supercomputer

- simulation. Biol Life Sci Forum 2024;35:5. doi:10.3390/blsf3500005
- [15]. Yedgar S., Barshtein G., Gural A., Hemolytic activity of nanoparticles as a marker of their hemocompatibility. Micromachines 2022;13:2091. doi:10.3390/mi13122091 [16]. Fedel M. Hemocompatibility of carbon nanostructures. C 2020;6:12. doi:10.3390/c6010012
- [17]. Youssry M., Al-Ruwaidhi M., Zakeri M., *Physical functionalization of multi-walled carbon nanotubes for enhanced dispersibility in aqueous medium*. Emergent Mater 2020;3:25–32. doi:10.1007/s42247-020-00076-3 [18]. Kutwin M., Sawosz E., Jaworski S., Kurantowicz N., Strojny B., Chwalibog A., *Structural damage of chicken red blood cells exposed to platinum nanoparticles and cisplatin*. Nanoscale Res Lett. 2014 May 23;9(1):257. doi: 10.1186/1556-276X-9-257
- [19]. Saha K., Moyano D.F., Rotello V.M., *Protein coronas suppress the hemolytic activity of hydrophilic and hydrophobic nanoparticles*. Mater Horiz 2014;1:102–105. doi:10.1039/C3MH00075C
- [20]. Yang K., Wan J., Zhang S., Tian B., Zhang Y., Liu Z., *The Influence of Surface Chemistry and Size of Nanoscale Graphene Oxide on Photothermal Therapy of Cancer Using Ultra-Low Laser Power*. Biomaterials 2012, 33, 2206–2214. https://doi.org/10.1016/j.biomaterials.2011.11.064 [21]. Bussy C., Ali-Boucetta H., Kostarelos K., *Safety Considerations for Graphene: Lessons Learnt from Carbon Nanotubes*. Acc. Chem. Res. 2013, 46, 692–701. https://doi.org/10.1021/ar3000452
- [22]. Zhang H., Lv X., Li Y., Wang Y., Li W., Chen J., Li Y., Surface Oxidation of Graphene Oxide Determines Membrane Damage, Lipid Peroxidation, and Cytotoxicity in Macrophages in a Pulmonary Toxicity Model. ACS Nano 2018, 12, 1390–1402. https://doi.org/10.1021/acsnano.7b07737 [23]. Syam Sundar L., Muhammad W.A., Synthesis and characterization methods of graphene oxide nanomaterial for biomedical and toxicity applications: A comprehensive review, Inorganic Chemistry Communications, Volume 174, Part 1, 2025, 113936, ISSN 1387-7003, https://doi.org/10.1016/j.inoche.2025.113936.
- [24]. Ghann, W.E.; Kang, H.; Uddin, J.; Chowdhury, F.A.; Khondaker, S.I.; Moniruzzaman, M.; Kabir, M.H.; Rahman, M.M., *Synthesis and Characterization of Reduced Graphene Oxide and Their Application in Dye-Sensitized Solar Cells*. ChemEngineering 2019, 3, 7. https://doi.org/10.3390/chemengineering3010007
- [25]. Kavinkumar T., Manivannan S., (2016). Synthesis, Characterization and Gas Sensing Properties of Graphene Oxide-Multi Walled Carbon Nanotube Composite. Journal of Materials Science & Technology. 32. 10.1016/j. jmst.2016.03.017.
- [26]. Yan X., Tang W., Cui H., Effect of MWCNTs-OH on the mechanical properties of cement composites: From macro to micro perspective, Construction and Building Materials, Volume 444, 2024, 137652, ISSN 0950-0618, https://doi.org/10.1016/j.conbuildmat.2024.137652. [27]. Dobrovolskaia M.A., Clogston J.D., Neun B.W., Hall J.B., Patri A.K., McNeil S.E., Method for analysis of

- nanoparticle hemolytic properties in vitro. Nano Lett. 2008 Aug;8(8):2180-7. doi: 10.1021/nl0805615.
- [28]. Jaworski S., Hinzmann M., Sawosz E., Grodzik M., Kutwin M., Wierzbicki M., Strojny B., Vadalasetty K.P., Lipińska L., Chwalibog A., *Interaction of different forms of graphene with chicken embryo red blood cells*. Environ Sci Pollut Res Int. 2017 Sep;24(27):21671-21679. doi: 10.1007/s11356-017-9788-5. Epub 2017 Jul 28. PMID: 28755146; PMCID: PMC5591802.
- [29]. Kroll A., Pillukat M.H., Hahn D., Schnekenburger J., Interference of engineered nanoparticles with in vitro toxicity assays. Arch Toxicol. 2012 Jul;86(7):1123-36. doi: 10.1007/s00204-012-0837-z. Epub 2012 Mar 11. [30]. Lophaisankit P., Boonyok K., Khonmee J., Udomtanakunchai C., Sodarat C., Phongroop K., Prachasilchai W., Feline Erythrocytic Osmotic Fragility in Normal and Anemic Cats—A Preliminary Study. Vet. Sci. 2025, 12, 236. https://doi.org/10.3390/vetsci12030236
- [31]. Christopher M.M., White J.G., Eaton J.W., *Erythrocyte pathology and mechanisms of Heinz body-mediated hemolysis in cats*. Vet Pathol 1990;27:299–310. doi:10.1177/030098589002700501
- [32]. Mukhopadhyay R., Lim H. G., Wortis M., Echinocyte Shapes: Bending, Stretching, and Shear Determine Spicule Shape and Spacing. Biophys. J. 2002, 82(4), 1756–1772. https://doi.org/10.1016/S0006-3495(02)75499-8 [33]. Tian Y., Tian Z., Dong Y., Wang X., Zhan L., Current advances in nanomaterials affecting morphology, structure, and function of erythrocytes. RSC Adv. 2021, 11, 6958–6971. https://doi.org/10.1039/D0RA10124A [34]. de la Harpe K.M., Kondiah P.P.D., Choonara Y.E., Marimuthu T., du Toit L.C., Pillay V., The Hemocompatibility of Nanoparticles: A Review of Cell–Nanoparticle Interactions and Hemostasis. Cells 2019, 8, 1209. https://doi.org/10.3390/cells8101209
- [35]. Mukhopadhyay R., Lim H. G., Wortis M., Echinocyte Shapes: Bending, Stretching, and Shear Determine Spicule Shape and Spacing. Biophys. J. 2002, 82(4), 1756–1772. https://doi.org/10.1016/S0006-3495(02)75499-8 [36]. Tian Y., Tian Z., Dong Y., Wang X., Zhan L., Current advances in nanomaterials affecting morphology, structure, and function of erythrocytes. RSC Adv. 2021, 11, 6958–6971. https://doi.org/10.1039/D0RA10124A [37]. De la Harpe K.M., Kondiah P.P.D., Choonara Y.E., Marimuthu T., du Toit L.C., Pillay V., The hemocompatibility of nanoparticles: a review of cell–nanoparticle interactions and hemostasis. Cells 2019;8:1209. doi:10.3390/cells8101209
- [38]. Zhao X., Liu R., Wang Z., Li T., Yan L., Li Y., *Effects of long and short carboxylated or aminated MWCNTs on red blood cells.* PLoS One 2012;7:e38995. doi:10.1371/journal.pone.0038995
- [39]. Strojny B., Kurantowicz N., Sawosz E., Grodzik M., Jaworski S., Kutwin M., Wierzbicki M., Hotowy A., Lipińska L., Chwalibog A., *Long-term influence of carbon nanoparticles on health and liver status in rats*. PLoS One 2015;10(12):e0144821. doi:10.1371/journal.pone.0144821